ACS APPLIED MATERIALS & INTERFACES

Subscriber access provided by CLEMSON UNIV

Energy, Environmental, and Catalysis Applications

Insights into the CO2 Stability-Performance Trade-off of Antimony-Doped SrFeO3-# Perovskite Cathode for Solid Oxide Fuel Cells

Yuqing Meng, Le Sun, Jun Gao, Wenzhou Tan, Chu-Sheng Chen,
Jianxin Yi, Henny Bouwmeester, Zhihu Sun, and Kyle Brinkman

ACS Appl. Mater. Interfaces, **Just Accepted Manuscript** • DOI: 10.1021/acsami.9b00876 • Publication Date (Web): 04 Mar 2019

Downloaded from http://pubs.acs.org on March 12, 2019

Just Accepted

“Just Accepted” manuscripts have been peer-reviewed and accepted for publication. They are posted online prior to technical editing, formatting for publication and author proofing. The American Chemical Society provides “Just Accepted” as a service to the research community to expedite the dissemination of scientific material as soon as possible after acceptance. “Just Accepted” manuscripts appear in full in PDF format accompanied by an HTML abstract. “Just Accepted” manuscripts have been fully peer reviewed, but should not be considered the official version of record. They are citable by the Digital Object Identifier (DOI®). “Just Accepted” is an optional service offered to authors. Therefore, the “Just Accepted” Web site may not include all articles that will be published in the journal. After a manuscript is technically edited and formatted, it will be removed from the “Just Accepted” Web site and published as an ASAP article. Note that technical editing may introduce minor changes to the manuscript text and/or graphics which could affect content, and all legal disclaimers and ethical guidelines that apply to the journal pertain. ACS cannot be held responsible for errors or consequences arising from the use of information contained in these “Just Accepted” manuscripts.

ACS Publications

is published by the American Chemical Society. 1155 Sixteenth Street N.W., Washington, DC 20036

Published by American Chemical Society. Copyright © American Chemical Society. However, no copyright claim is made to original U.S. Government works, or works produced by employees of any Commonwealth realm Crown government in the course of their duties.

Insights into the CO_2 Stability-Performance Trade-off of Antimony-Doped $SrFeO_{3-\delta}$ Perovskite Cathode for Solid Oxide Fuel Cells

Yuqing Meng[†], Le Sun[†], Jun Gao[#], Wenzhou Tan[†], Chusheng Chen[†], Jianxin Yi[‡, *], Henny J. M. Bouwmeester[†, §], Zhihu Sun[¶], and Kyle S. Brinkman[#]

[†] *CAS Key Laboratory of Materials for Energy Conversion, Collaborative Innovation Center of Chemistry for Energy Materials and Department of Materials Science and Engineering, University of Science and Technology of China, Hefei 230026, China*

[‡] *State Key Laboratory of Fire Science, Department of Safety Science and Engineering, University of Science and Technology of China, Hefei 230026, China*

[#] *Department of Materials Science and Engineering, Clemson University, Clemson, SC 29634, USA*

[§] *Electrochemistry Research Group, Faculty of Science and Technology, MESA+ institute for nanotechnology, University of Twente, 7500 AE The Netherlands*

[¶] *National Synchrotron Radiation Laboratory, University of Science and Technology of China, Hefei 230029, China*

[*] Corresponding author. E-mail: yjx@ustc.edu.cn (J. Yi).

Abstract

One major challenge for the further development of solid oxide fuel cells is to obtain high performance cathode materials with sufficient stability against reactions with CO_2 present in the ambient atmosphere. However, the enhanced stability is often achieved by using material systems exhibiting decreased performance metrics. The phenomena underlying the performance and stability trade-off has not been well understood. This paper uses antimony-doped $SrFeO_{3-\delta}$ as a model material to shed light on the relationship between structure, stability, and performance of perovskite structured oxides which are commonly used as cathode materials. X-ray absorption revealed that partial substitution of Fe by Sb leads to a series of changes in the local environment of the iron atom, such as a decrease in the iron oxidation state and an increase in the oxygen coordination number. Theoretical calculations show that the structural changes are associated with an increase in both the oxygen vacancy formation energy and the metal-oxygen bond energy. The area specific resistance of the perovskite oxide increases with Sb doping, indicating a deterioration of the oxygen reduction activity. Exposure of the materials to CO_2 leads to depressed oxygen desorption and an increased area specific resistance, which becomes less pronounced at higher Sb doping levels. Origin of the stability-performance trade-off is discussed based on the structural parameters.

KEYWORDS: *solid oxide fuel cells, cathode, CO_2 tolerance, ORR, XAFS*

1. INTRODUCTION

Solid oxide fuel cells (SOFC) are a promising alternative energy device that converts the chemical energy of a fuel (such as hydrogen or methane) directly into electricity. Due to their excellent fuel flexibility, SOFCs can also serve as an economic bridge for a potential transition from a fossil-fuel-based economy to a renewable hydrogen-fuel-based economy.[1] Currently, there are still a number of inherent challenges for the development of SOFC technology, such as understanding and mitigating performance degradation, management of mechanical stresses and high temperature gas-tight sealing. During SOFC operation, cathode materials may be poisoned by aggressive gases present in the ambient air, such as CO_2, which lead to a significant degradation of performance[2,3]. The sensitivity of the cathode materials to CO_2 poisoning is due to the adsorption of CO_2 or the formation of carbonate species on the material surface, which may alter the original phase structure and result in a significant impact on the surface oxygen exchange. A cathode material with good CO_2 tolerance would be of immense practical value for the application of SOFCs.

State-of-the-art cathode materials are predominantly based on mixed ionic-electronic conducting (MIEC) perovskite oxides due to their excellent activity towards the oxygen reduction reaction (ORR). Numerous studies have shown that the ORR activity of these materials is susceptible to even small amounts of CO_2 [4,5,6], which have been ascribed to the basic nature of the contained alkaline-earth elements.[7,8] The CO_2 resistance of the MIEC perovskite oxides can be improved by partial substitution of the A- and/or B-site cations with higher valent cations. Examples include partial substitution of the B-site transition metal cations with Ti^{4+}, Zr^{4+}, Ta^{5+}, and Sb^{5+} for $SrCo_{0.8}Fe_{0.2}O_{3-\delta}$[8], $SrFeO_{3-\delta}$[9,10], $BaCo_{1-x}Fe_xO_{3-\delta}$[11], $SrSc_{0.1}Fe_{0.9}O_{3-\delta}$[12] and $La_{0.6}Sr_{0.4}FeO_{3-\delta}$[13], and of the A-site alkaline-earth cations with La^{3+} for $SrCo_{0.8}Fe_{0.2}O_{3-\delta}$[14], Ca^{2+} for $LaFeO_{3-\delta}$[15]. An increase in the acidity and the thermodynamic stability of the perovskite oxides have been proposed to account for the enhanced CO_2 resistance[16,10]. Unfortunately, the doping of higher valent cations often leads to deterioration of the oxygen transport properties. Schulze-Kuppers *et al.*[17] found that the oxygen permeation property dropped by partial substitution of Fe by Ti in strontium ferrite. Chen *et al.*[18] found that Ta^{5+} doping in B-site of $SrCo_{0.8}Fe_{0.2}O_{3-\delta}$ enhanced the phase stability but also resulted in the degradation of the oxygen permeation flux. Han *et al.*[19] improved the CO_2 resistance of $SrFeO_{3-\delta}$ with Nb doping which may be related to the increased metal-oxygen bonding. Similar tuning of the materials property via cation doping has also been studied for various applications[20, 21].

Insight into the stability-performance trade-off relationship is vital to rational design of new electrode materials with both high ORR activity and CO_2 tolerance. Some efforts have been devoted to exploring the governing factors for these properties. Zhu et al[22] investigated the CO_2 resistance of $SrNb_{0.1}Co_{0.9-x}Fe_xO_{3-\delta}$ and found that oxygen vacancies can promote the formation of carbonates. The oxygen reduction activity is related to the oxygen vacancy concentration (nonstiochiometry)[23], energies for oxygen migration and oxygen vacancy formation[24]. Zhang et al[25] found that the CO_2 tolerance of $SrSc_{0.175}Nb_{0.025}Co_{0.8}O_{3-\delta}$ cathode could be related to the higher average metal-oxygen bond energy (ABE) and higher acidity of Nb^{5+} cations. Huang et al[26] found that CO_2 competes with O_2 for binding to vacancy sites on $Ba_{0.5}Sr_{0.5}Co_{0.8}Fe_{0.2}O_{3-\delta}$ (BSCF), thus inhibiting the interaction between O_2 and the solid surface.

Nevertheless, a clear understanding how both properties can be tuned in perovskite structured cathodes is still missing. It is worth noting that, both the CO_2 resistance and oxygen reduction activity are strongly correlated to the intrinsic structural parameters (such as oxygen vacancy concentration) and the chemical identity of dopant elements.

Herein, we report on a systematic investigation of the structure, ORR, and CO_2 resistance of a model material, Sb-doped $SrFeO_{3-\delta}$. Changes in the local structure around the Fe atoms in the perovskites were probed by synchrotron radiation X-ray absorption spectroscopy (XAS) combined with density functional theory (DFT) calculations. The effect of CO_2 on the structure and oxygen transport properties was studied with a number of techniques including temperature programmed desorption (TPD), electrical conductivity relaxation (ECR), and impedance spectroscopy. The structural origin of the trade-off between stability and performance is discussed. This work aims to provide fundamental insights into the ORR activity and CO_2 tolerance for perovskite oxides, and results obtained can be applied to the design of SOFC cathode materials.

2. EXPERIMENTAL SECTION

$SrFe_{1-x}Sb_xO_{3-\delta}$ (x=0, 0.05, 0.10, 0.15, 0.20, denoted as $SrFeO_3$, SFS05, SFS10, SFS15, SFS20) powders were synthesized by solid state reaction. Stoichiometric amounts of $SrCO_3$ (AR, Sinopharm Chemical Reagent Co., China), Fe_2O_3 (AR, Sinopharm Chemical Reagent Co., China), Sb_2O_5 (AR, Sinopharm Chemical Reagent Co., China) were ball-milled, calcined in air at 1200 °C for 10 h, and furnace-cooled to room temperature. In addition, in order to investigate the oxygen nonstoichiometry under different atmospheres, SFS20 powder samples were annealed under nitrogen and quenched in air from 900 °C, respectively.

The phase structure of the as-prepared and CO_2-treated powders were analyzed by X-ray diffraction (XRD). The data were collected at room temperature and in ambient air with a diffractometer (X'Pert Pro, Phillips, Netherlands) using Cu/kα radiation (λ = 1.54108 Å), with a scan range of 20-80º and a step size of 0.02º. *In-situ* high-temperature XRD was conducted in air with a heating rate of 5 ºC min^{-1}. X-ray photoelectron spectroscopy (XPS) was conducted on an ESCALAB 250 spectrometer (Thermo-VG Scientific).

Fe K-edge XAS spectra of SFS powders were recorded at room temperature in the transition mode at the beamline BL14W1 of the Shanghai Synchrotron Radiation Facility (SSRF). The beamline provides a focused monochromatic X-ray source of 2.5 GeV with a Si⟨111⟩ monochromator. The X-ray energy was calibrated by using an Fe foil. The acquired data were processed according to standard procedures using the ATHENA module[27]. Extended x-ray absorption fine structure (EXAFS) was analyzed using the ARTEMIS module implemented in the IFEFFIT software packages[28]. Commercial powders of FeO, (99.7%, Alfa Aesar), Fe_2O_3 (99.9%, Alfa Aesar) and Fe_3O_4 (99.6%, Sinopharm Chemical Reagent Co., China) were used as reference oxides.

Density functional theory calculations were carried out using the Vienna ab initio simulation package (VASP)[29, 30]. The kinetic energy cut-off was 700 eV, and the energy convergence criterion was 10^{-5} eV. The Hellmann-Feynman force on each atom was smaller than 0.03 eV/Å. In addition, the DFT+U method was applied to the Fe cations with U_{eff} of 5.3 eV. A 2 × 2 × 2 supercell with *k*-point grid 5 × 5 × 5 was adopted for calculation of the oxygen vacancy formation energy. The oxygen vacancy formation energy was calculated based on the formula $E_{vac} = E[\text{defect}] + 1/2E[O_2] - E[\text{perfect}]$, where E[defect] and E[perfect] are the total energies of defective and ideal $SrFeO_3$. $E[O_2]$ is the total energy of O_2 in the triplet state.

TPD measurements were conducted on 100 mg powders in a U-shaped quartz tube. Prior to the measurements, the powders were pre-treated in CO_2 at 800 °C for 5 h, and subsequently annealed in air at 450 °C for 40 min, followed by 30 min annealing in an Ar stream. The samples were then heated in an Ar carrier gas stream to 1000 °C with a heating rate of 10 °C min^{-1}, and held at that temperature until desorption/release was complete. The O_2 and CO_2 signals were monitored with a mass spectrometer (QIC20, Hiden). O_2-TPD measurements were conducted on fresh samples of SFS05 and SFS20. These samples were pretreated in Helium for 30 mins at room temperature, which were heated directly to 1000 °C in Ar or CO_2 carrier gas streams, without the CO_2 pre-treatment.

The ECR method was applied to determine the oxygen surface exchange rate in the presence of CO_2. The SFS powders were pressed into rectangular bars at 300 MPa and sintered in air to form dense pellets. The relative density is over 94% of the theoretical density. The sintered bars had dimensions of approximately $15.0 \times 6.0 \times 1.2$ mm^3. The conductivity was measured using the four-probe method with a digital multimeter (Keithley, 2001 multimeter). Changes in gas compositions were realized in less than 1 s at a gas flow rate of 300 ml min^{-1} using the O_2-N_2 mixture with oxygen partial pressure (pO_2) range from 0.005 to 0.1 atm. The electrical conductivity changed continuously with time and reached a new equilibrium point when the atmosphere was abruptly changed.

For the fabrication of symmetrical cells, $Ce_{0.8}Gd_{0.2}O_{1.9}$ (GDC20) pellets were prepared by uniaxially pressing GDC20 powders (Fuelcell Materials, US) followed by sintering at 1450 °C for 5 h. The SFS slurry was prepared by mixing the electrode powder with organics (20 wt.% solsperse 28000 (Lubrizol) dissolved in terpinol), and binder (5 wt.% V-006 (Heraeus) dissolved in terpinol). The cathode slurry was printed on both sides of GDC20 pellet, then fired at 1000 °C for 2 h. For the single cell fabrication, a NiO/GDC20 anode support was first fabricated and pre-fired at 1000 °C for 2 h. A GDC electrolyte layer was deposited on the anode support by a particle suspension coating process followed by co-firing at 1450 °C for 5 h. The SFS slurry was screen-printed onto the surface of GDC20 electrolyte, and then co-fired at 1000 °C for 2 h to form a porous cathode (with an area of 0.385 cm^2). The area specific resistance (ASR) of the cathodes was measured in a two-electrode symmetrical cell configuration with Ag paste as current collector on both sides. The Impedance spectra were measured using a Solartron 1260 electrochemical workstation with an AC amplitude of 10 mV in the frequency range from 1 M Hz to 0.01 Hz. The single cells were tested under wet H_2 for anode and ambient air for cathode.

3. RESULTS AND DISCUSSION

3.1 Structure

The X-ray diffraction patterns of the as-prepared SFS powders are displayed in Figure 1. Rietveld refinements of the patterns reveal that the diffraction peaks obtained for each sample can be indexed on the basis of a cubic perovskite structure (space group *Pm-3m)*. No evidence of impurity phases is observed. The lattice parameters extracted from the Rietveld refinements are found to increase linearly with the Sb content, indicative of formation of $SrFe_{1-x}Sb_xO_{3-\delta}$ solid solutions according to Vegard's law[31]. *In-situ* high-temperature XRD on SFS10 shows that the perovskite structure is maintained upon heating to 1000 °C in ambient air (Figure S1). The dilatometric analysis shows a variation in the slope for all the compositions at ~582 ºC (Figure S2), which could be related to the oxygen losses after heating[32]. The TEC values decrease with an increase of the Sb content (Table S1), which are 34.5× 10^{-6} K^{-1} and 17.8× 10^{-6} K^{-1} for SFS05 and SFS20 above 582 ºC, respectively.

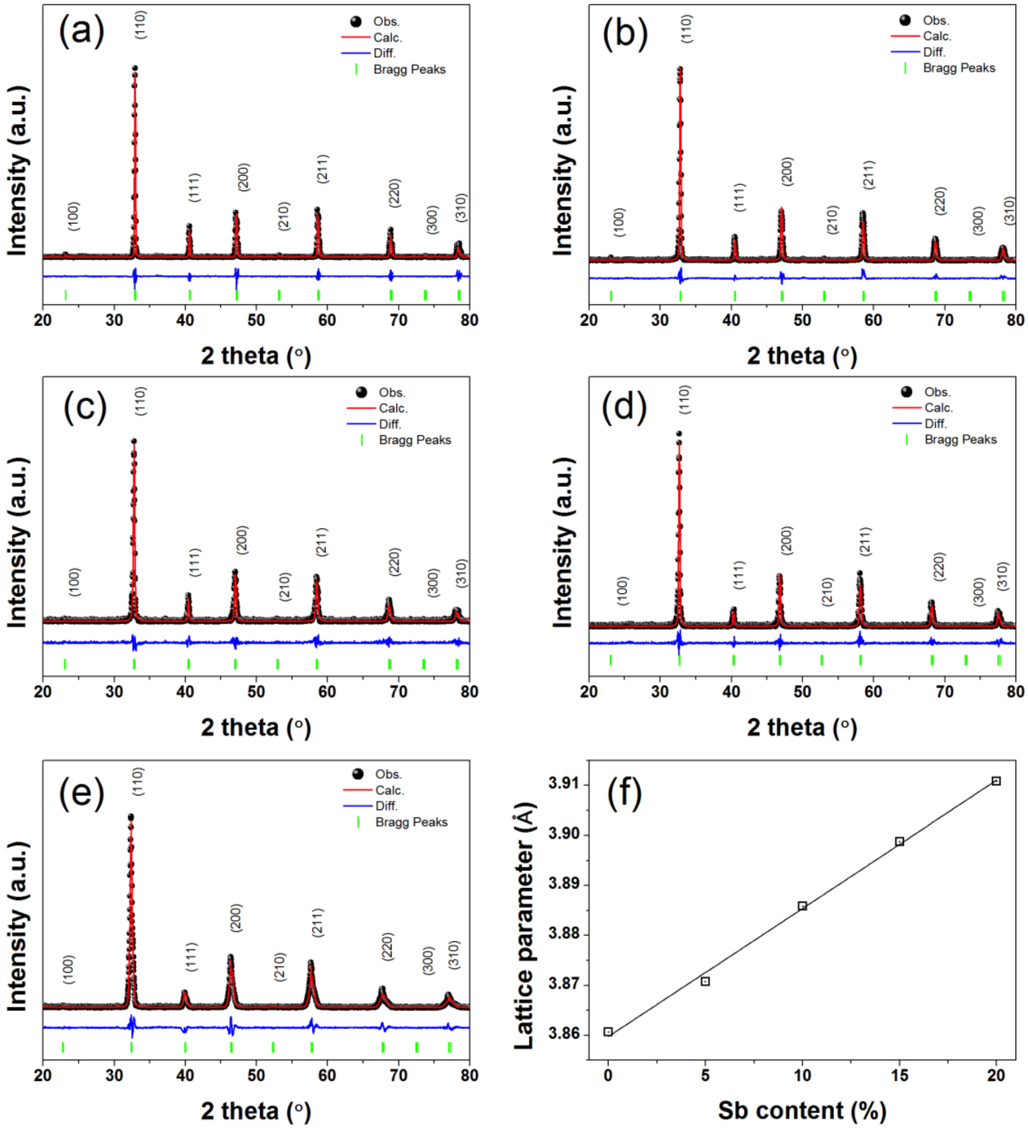

Figure 1. X-ray powder diffraction patterns and Rietveld refinements (red line) of (a) $SrFeO_3$, (b) SFS05, (c) SFS10, (d) SFS15, and (e) SFS20, and (f) lattice parameter as a function of Sb content.

The O1s and Fe2p XPS spectra for the SFS series are shown in Figure 2a and 2b, respectively. The O1s peak for the undoped material (x = 0) can be de-convoluted into three Gaussian peaks. Peak centered at 533.6 eV is assigned to absorbed water, whereas peaks centered at 531.3 eV and 528.1 eV are assigned to absorbed oxygen[8] and lattice oxygen, respectively. The O1s peaks overlap with the two Sb 3d peaks in the spectra for the Sb-doped samples. Deconvolution of the spectra shows that the lattice oxygen peak shifts to higher BE with increasing Sb content (Figure 2c), suggesting a decrease of the surface basicity with increasing Sb doping[33]. The Fe2p XPS spectra for the series (Figure 2b) consist of $2p_{3/2}$ and 2p1/2 doublets and a satellite peak at 717.9 eV. The $2p_{3/2}$ doublet can be deconvoluted into two peaks at 710.1 eV and 711.6 eV, corresponding to Fe^{3+} and Fe^{4+}, respectively. Similar behavior is observed for the $2p_{1/2}$ doublet, indicating that iron in the SFS perovskites is present as a mixture of Fe^{3+} and Fe^{4+}. The average valence of the iron cations was estimated from the area ratio of the Fe^{3+} and Fe^{4+} peaks, and the average valence was found to decrease slightly from 3.5 to 3.4 with increasing Sb content (Figure 2c).

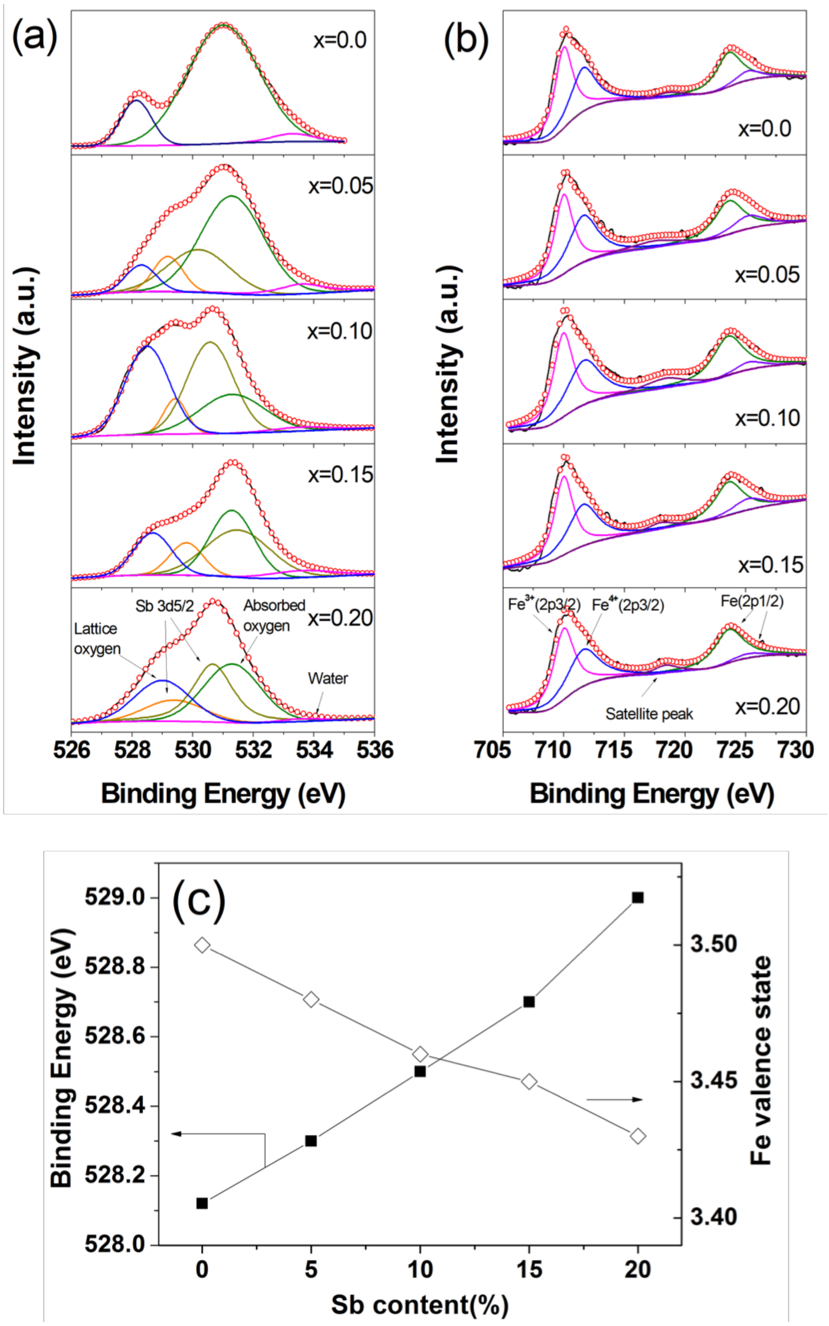

Figure 2. (a) O1s and (b) Fe 2p XPS spectra for the series $SrFe_{1-x}Sb_xO_{3-\delta}$ (x=0, 0.05, 0.10, 0.15, 0.20), and (c) binding energy of lattice oxygen and Fe valence state as a function of Sb content.

X-ray absorption measurements were performed to probe the local structure around the iron cations in the SFS perovskite series. Figure 3a shows the X-ray absorption near edge structure (XANES) spectra at the Fe K-edge for the SFS perovskites and reference oxides (FeO, Fe_2O_3 and Fe_3O_4) recorded at room temperature. All spectra consist of a small pre-edge peak at around 7112 eV, corresponding to the transition from the deep 1s core level to the 3d quasi-bound state[34]. The intensity of the pre-edge peak is an indication of the crystal symmetry.[35,36,37] The pre-edge peaks can be deconvoluted into two peaks (Figure S3), which can be assigned to FeO_6 octahedra (O_h) at the higher energy and FeO_5 pyramid at the lower energy.[38] With increasing Sb content, the relative intensity of the O_h peak increases while the FeO_5 peak decreases (Table 1), indicating that more iron cations adopt an octahedral coordination. Note that for the SFS20 samples subjected to quenching after high temperature annealing in air or to annealing in N_2, a significantly smaller O_h intensity was obtained as compared with the SFS20 sample annealed in air. This observation indicates that the distribution of iron cations over FeO_5 sites and FeO_6 octahedral sites is strongly influenced by the heat-treatment history, which may result from a change of oxygen nonstoichiometry.

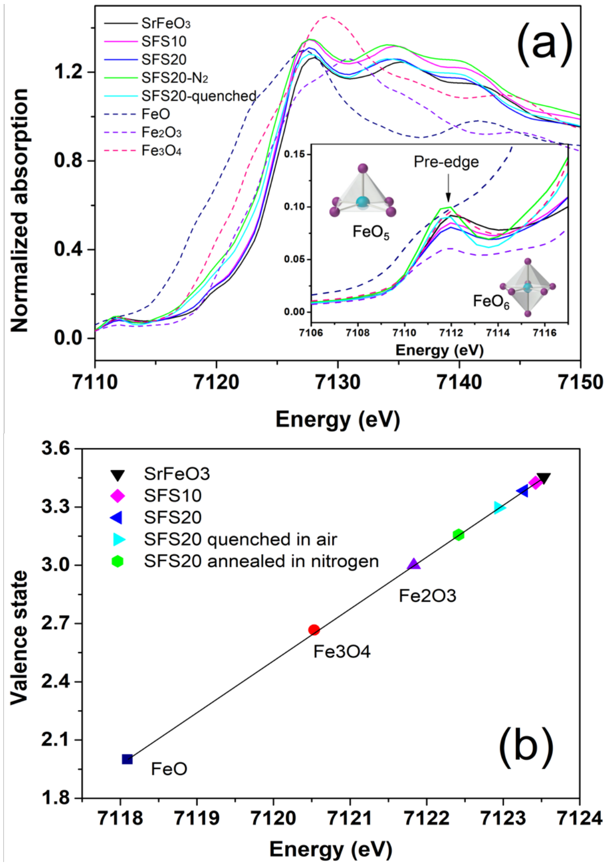

Figure 3. (a) Normalized room temperature Fe K-edge XANES spectra of SFS samples and reference oxides. Inset shows a magnified view of the Fe pre-edge peaks. (b) Average valence

states of iron cation in $SrFe_{1-x}Sb_xO_{3-\delta}$ (x=0, 0.10, 0.20) powders and reference oxides FeO, Fe_3O_4, and Fe_2O_3.

Table 1. Peak intensity of the different Fe configurations for $SrFe_{1-x}Sb_xO_{3-\delta}$ (x=0, 0.10, 0.20) .

Sample	$SrFeO_3$	SFS10	SFS20	SFS20-N_2	SFS20-quenched
FeO_5	0.346	0.308	0.289	0.561	0.512
FeO_6	0.654	0.692	0.711	0.439	0.488

The absorption edge positions were determined as the energy at half the step height of the normalized curves. The K-edge energies for the SFS samples are larger than that for Fe_2O_3, indicating that iron cations in SFS adopt an average oxidation state higher than 3+ due to the coexistence Fe^{3+} and Fe^{4+}. The average Fe oxidation states of SFS were estimated by linear extrapolation of those for the reference oxides (Figure 3b). The oxidation states were found to decrease slightly with increasing Sb content, in agreement with the XPS results (Figure 2). Assuming an oxidation state of 5+ for Sb, the oxygen nonstoichiometry was then estimated and found to decrease from 0.25 for x=0 to 0.13 for x = 0.2 (SFS20). A significantly lower iron oxidation state and thus larger oxygen nonstoichiometry was observed for the quenched (δ=0.18) or N_2-annealed (δ=0.24) SFS20 samples. These results agree well with the observed change of O_h intensity in Figure 3a.

The room-temperature Fe K-edge EXAFS spectra (***k*** range 2.68 - 13.2 $Å^{-1}$) were Fourier-transformed to the radial distribution function (RDF), as shown in Figure 4. The FT magnitude in the range of 1.0-1.8 Å corresponds to the Fe-O bond, while the other two FT magnitudes in the range of 2.6-3.8 Å can be assigned to Fe-Sr and Fe-Fe/Fe-Sb bonds. The simulated Fourier-transformed EXAFS spectra fit very well to the experimental data (Figure S5). Structural parameters for $SrFe_{1-x}Sb_xO_{3-\delta}$ (x=0, 0.10, 0.20) extracted from analysis are presented in Table 2. The number of oxygen anions in the first coordination shell of the Fe cations was found to increase with Sb doping, which is consistent with the increase of δ with Sb doping (shown in XANES results). The Fe-O and Fe-Sr interatomic distances increase with Sb doping, which is in line with the lattice expansion found by XRD (Figure 1). The increase of the interatomic distances is associated with an increase of the Debye-Waller (DW) factor[39], which is indicative of enhanced thermal and structural disorder. The Fe-Sb distances in both SFS10 and SFS20 are found slightly larger than the corresponding Fe-Fe distances, suggesting presence of some local structural distortion in both materials. This slight change was not observed from the XRD patterns in Figure 1, which may suggest that the EXAFS is more sensitive to changes of cation local structures.

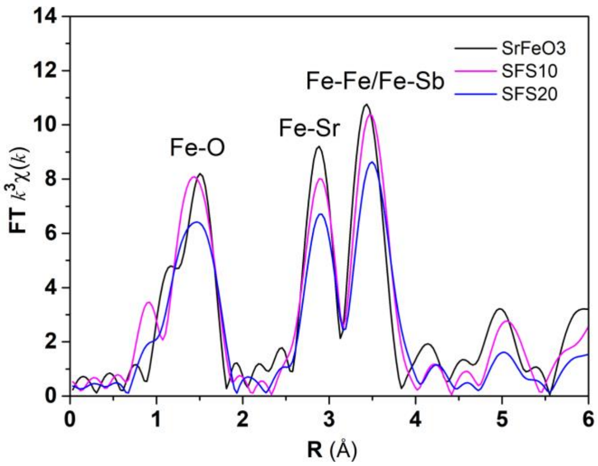

Figure 4. Fourier transform (FT) magnitudes of the Fe-edge EXAFS oscillations for $SrFe_{1-x}Sb_xO_{3-\delta}$ (x=0, 0.10, 0.20).

Table 2. Structural parameters from EXAFS spectra analyses for $SrFe_{1-x}Sb_xO_{3-\delta}$ (x=0, 0.10, 0.20). Coordination number N, amplitude reduction factor S_o^2, interatomic distance R, Debye-Waller factor σ^2, and goodness-of-fit R-factor.

Sb fraction	**Path**	***N***	S_o^2	***R* (Å)**	σ^2 (×10^{-3} Å^2)	**R-factor**
0.00	Fe-O	5.1	0.7	1.92	5.87	0.013
	Fe-Sr	8.0		3.30	6.98	
	Fe-Fe	6.0		3.84	6.20	
0.10	Fe-O	5.3	0.7	1.94	5.97	0.015
	Fe-Sr	8.0		3.34	7.31	
	Fe-Fe	5.4		3.88	8.43	
	Fe-Sb	0.6		4.01	11.56	
0.20	Fe-O	5.8	0.7	1.95	8.37	0.009
	Fe-Sr	8.0		3.35	10.36	
	Fe-Fe	4.8		3.89	8.80	
	Fe-Sb	1.2		4.01	11.30	

First-principle calculations were performed to assess the influence of Sb doping on the oxygen vacancy formation energy in $SrFe_{1-x}Sb_xO_{3-\delta}$. Possible sites are depicted in Figure 5, wherein *a*1 denotes oxygen in Fe-O-Fe bonds of undoped $SrFeO_3$, and *b*1 and *b*2 denote oxygen in Fe-O-Fe and Fe-O-Sb bonds in Sb-doped $SrFeO_3$, respectively. The energy required for the formation of oxygen vacancies at *b*1 sites in the doped material equals 0.98 eV, which is close to 0.96 eV found for *a*1 sites in the undoped material, but distinctly lower than 1.68 eV for *b*2 sites. These results clearly indicate that oxygen bound to Sb cations are more stable than those bound to Fe, and oxygen vacancies would prefer to be formed between two adjacent Fe cations.

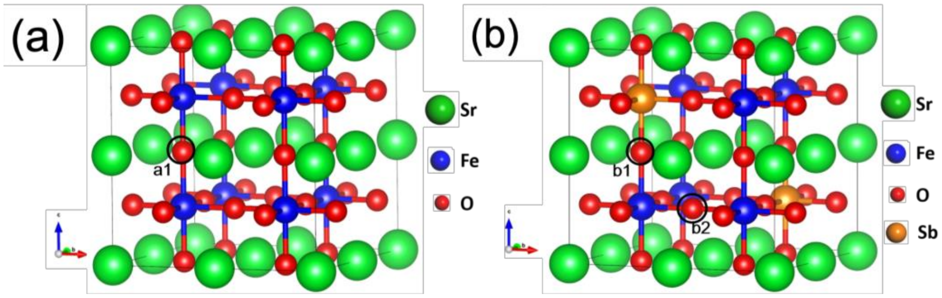

Figure 5. Schematic representation of oxygen vacancy formation in (a) $SrFeO_3$ and (b) Sb-doped $SrFeO_3$.

To further evaluate the influence of Sb doping on the perovskite structure stability, the average metal-oxygen bond energy (ABE) was calculated for $SrFe_{1-x}Sb_xO_{3-\delta}$ according to[19]

$$ABE = \frac{1}{12}\left(\Delta H_{\mathrm{SrO}} - \Delta H_{\mathrm{Sr}} - \frac{1}{2}D_{\mathrm{O_2}}\right) + \frac{1-x}{12}\left(\Delta H_{\mathrm{Fe_2O_3}} - 2\Delta H_{\mathrm{Fe}} - \frac{3}{2}D_{\mathrm{O_2}}\right) + \frac{x}{12}(\Delta H_{\mathrm{Sb_2O_5}} - 2\Delta H_{\mathrm{Sb}} - \frac{5}{2}D_{\mathrm{O_2}})$$

where ΔH_{SrO}, $\Delta H_{\mathrm{Fe_2O_3}}$ and $\Delta H_{\mathrm{Sb_2O_5}}$ are the heats of formation of SrO, Fe_2O_3 and Sb_2O_5, respectively; ΔH_{Sr}, ΔH_{Fe}, ΔH_{Sb} are the heats of sublimation of metals Sr, Fe, and Sb, respectively, and $D_{\mathrm{O_2}}$ is the dissociation energy of gaseous oxygen. As shown in Figure 6, the ABE becomes larger (more negative) with Sb substitution for Fe, indicating enhanced stability of the perovskite structure.

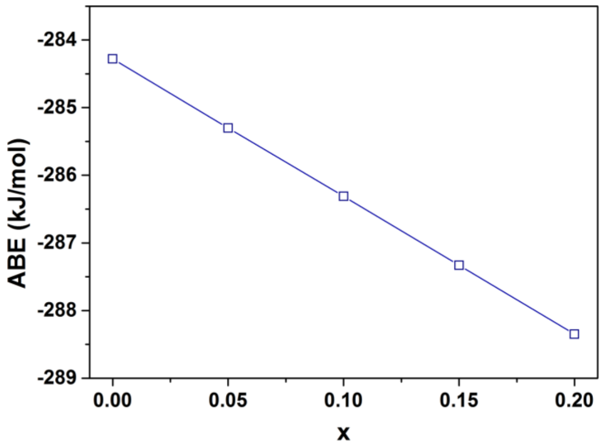

Figure 6. Average metal-oxygen bond energy (ABE) as a function of Sb content.

3.2 CO_2 tolerance and oxygen transport property

Figure 7 shows diffraction patterns of the SFS powders annealed in 1 bar CO_2 at 800 °C for 5 h. Presence of $SrCO_3$ was observed for SFS samples with x = 0 - 0.10, but not for samples x = 0.15 and x = 0.20. Isothermal TG measurements in CO_2 for x = 0.20 (SFS20) sample reveals that the sample weight remained almost constant at 900 °C within the experimental period (20 h), but slowly increased with time at 800 °C (Figure S6). These results indicate that carbonation reaction still took place at 800 °C for SFS20 but occurred at a relatively slow rate. The absence of carbonate in Figure 7 was probably due to the small amount formed after 5 h.

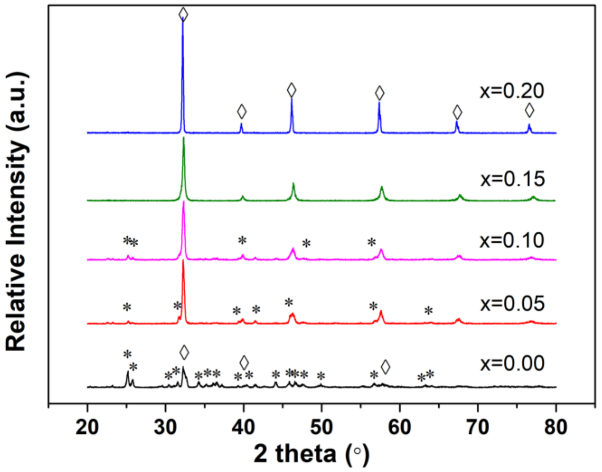

Figure 7. Room temperature X-ray powder diffraction patterns of $SrFe_{1-x}Sb_xO_{3-\delta}$ (x=0, 0.05, 0.10, 0.15, 0.20) after treatment in pure CO_2 at 800 °C for 5 h. Reflections of the perovskite (◊) and $SrCO_3$ (∗) phases are marked.

TPD spectra for the SFS powders pre-treated in CO_2 at 800 °C for 5 h are shown in Figure 8. CO_2 desorption (Figure 8a), indicative of the decomposition of $SrCO_3$ carbonate, occurred in the range of 500 – 880 °C. Oxygen release occurred over a much broader temperature range starting from ~370 °C (Figure 8b). This broad O_2 peak can be ascribed to the α-O_2 peak[40], which results from desorption of the chemisorbed oxygen on the surface and reduction of Fe^{4+} to Fe^{3+}. The O_2-peak intensity decreases with the increases of Sb doping level, agrees well with the decreased valence state of iron, as revealed by XPS and XANES. Both CO_2 and O_2 desorption became less pronounced with increasing Sb content, suggesting that Sb doping not only enhances the CO_2 resistance, but also reduces oxygen nonstoichiometry. According to Figure 8c, the O_2/CO_2 peak area ratio increases distinctly with Sb doping.

In order to examine the impact of CO_2 on the oxygen desorption, pristine SFS05 and SFS20 powder samples were studied with TPD in Ar or CO_2 carrier gas (Figure 8d), without being subjected to a CO_2 pre-treatment. Similar to Figure 8b, large O_2 desorption peaks were observed in Ar starting from ~360-400 °C. In contrast, as the carrier gas was changed to CO_2, the onset temperature for oxygen desorption was significantly shifted to 650 °C for SFS05 and 500 °C for SFS20. Moreover, both oxygen desorption peaks became smaller in CO_2, corresponding to 62.0% and 35.7% reduction of the peak area for SFS05 and SFS20, respectively. Apparently, the presence of CO_2 markedly inhibits the desorption of oxygen for both SFS05 and SFS20, with the reduction being more pronounced for the former. These findings are in good agreement with recent results of isotopic exchange experiments[26], which showed that CO_2 preferably adsorbs on BSCF perovskite surface and inhibits oxygen surface exchange.

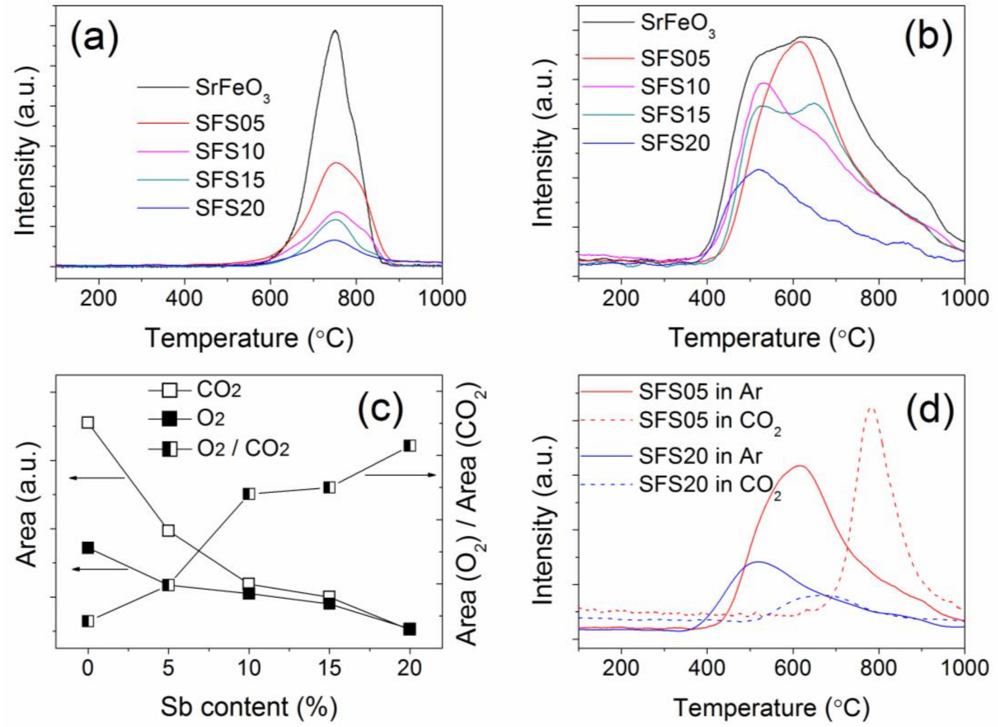

Figure 8. (a) CO_2-TPD curves, (b) O_2-TPD curves, and (c) the desorption peak areas of SFS powders treated in 1 atm CO_2 at 800 °C for 5h; (d) O_2-TPD of SFS05 and SFS20 using Ar or CO_2 as carrier gas.

The oxygen transport property was characterized by oxygen permeation experiments and impedance spectroscopy. For the oxygen permeation measurements, dense SFS ceramic membranes (Figure S8) were used, with one side exposed to air and the other side to He. As shown in Figure S9 and Table S2, the oxygen fluxes decrease while the associated activation energies increase with increasing Sb content. The area-specific resistance (ASR) was determined from the diameter of the impedance semicircle for the SFS symmetrical cells. The ASR of SFS cathode is larger than that of undoped $SrFeO_3$ (~0.044 Ω cm^2)[41], and increases from 0.11 Ω cm^2 to 0.13 Ω cm^2 as the Sb content increases at 800 °C in air (Figure 9). Clearly, Sb doping is detrimental to both the oxygen permeation and ORR activity of the $SrFeO_{3-\delta}$ perovskite.

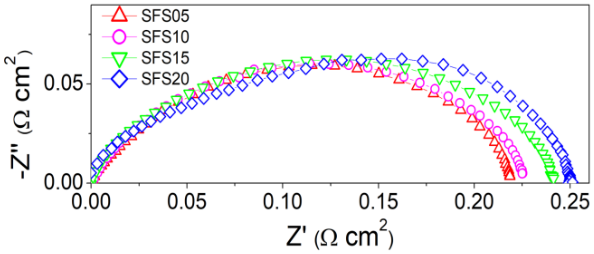

Figure 9. Impedance spectra of SFS symmetric cells measured at 800 °C in air. The ohmic resistance has been subtracted for the sake of simplicity.

The impact of CO_2 presence on the oxygen transport property was studied by monitoring the variation of the ASR of the SFS symmetrical cells upon exposure to CO_2 at 800 °C. Figure

10a shows that all the samples are susceptible to CO_2 presence and exhibit increased ASR. The time-dependent ASR plots agree well with a power law relationship, reflecting more pronounced degradation at the beginning of the CO_2 exposure but a much slower degradation rate at later times. Samples with higher Sb contents show significantly slower ASR degradation. For instance, the ASR of SFS05 increases rapidly by 4.2 times from 0.11 Ω cm^2 to 0.46 Ω cm^2 within 50 h. In contrast, the ASR of SFS20 electrode increases by only 40% within the same duration, and 64% of the ASR increase by 1000 h occurred within the initial 150 h. For comparison, we also measure the ASR of $La_{0.6}Sr_{0.4}Co_{0.2}Fe_{0.8}O_{3-\delta}$ (LSCF), a well-studied cathode material. It can be seen that although LSCF exhibits a smaller starting ASR (measured in air) than SFS20, it is more susceptible to CO_2 and the ASR exceeds that of SFS20 within 20 h. Figure 10b shows that the ASR of SFS20 increased gradually from 0.13 Ω cm^2 to 0.18 Ω cm^2 as the CO_2 concentration increases to 52%. Similar behavior was also observed for the oxygen surface exchange coefficient, K_{chem}. As evidenced by the ECR experiments in Figure S7, the K_{chem} value for SFS05 decreases from 4.3×10^{-4} cm s^{-1} in air to 3.7×10^{-4} cm s^{-1}, 2.3×10^{-4} cm s^{-1}, and 2.0×10^{-4} cm s^{-1} in 5%, 25%, and 52% CO_2, respectively. These results suggest that when the SFS samples are operated in realistic SOFC atmosphere (ambient air), less degradation was observed due to the lower CO_2 concentration (0.04%) as compared to the levels used in the present work.

Considering that SFS20 has excellent CO_2 tolerance, we constructed a single cell as a simple demonstration of the performance of SFS20 as the cathode. The 20 μm-thick cathode exhibits uniform porosity and adheres well with the 15 μm-thick GDC20 electrolyte (Figure S10). Figure 11 displays the *IVP* curves of the single cells tested at 650-800 °C using humidified H_2 (~3% H_2O) as fuel and ambient air as an oxidant. At 650 °C, a peak powder density of ~245 mW cm^{-2} was achieved, which is comparable to that of a single cell with a $Sm_{0.5}Sr_{0.5}CoO_{3-\delta}$ cathode[42]. Note that the cell performance can in principle be substantially enhanced by optimizing the materials and microstructure, e.g., using cathode of higher ORR activity and/or thinner electrolyte.

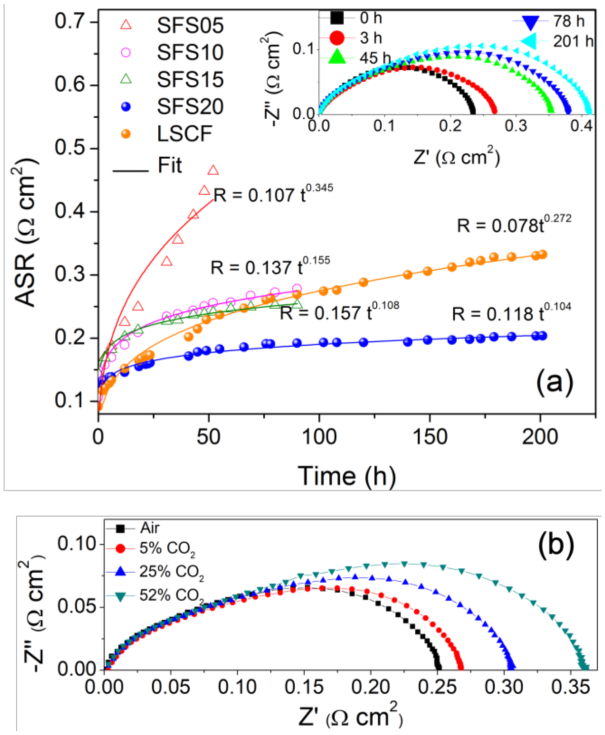

Figure 10. (a) Durability of SFS and LSCF symmetric cells in air with 1% CO_2 at 800 ºC, inset is the EIS of the SFS20 symmetric cell. (b) Impedance spectra of SFS20 symmetric cell measured at 800 ºC with different CO_2 concentration. PO_2 was kept at 0.21 atm.

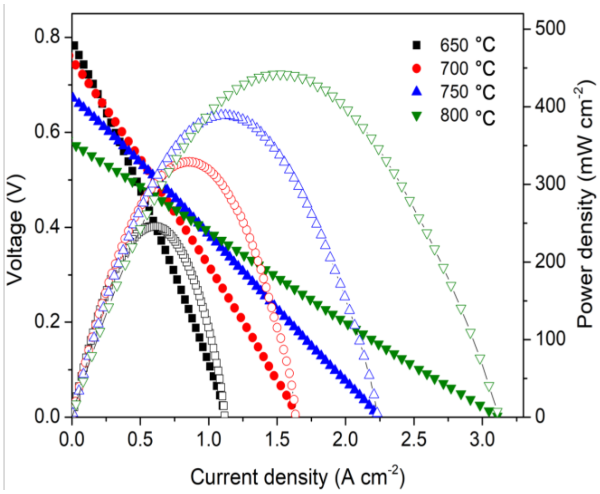

Figure 11. Current-voltage characteristics and corresponding power density of the single cell.

3.3 Structure-property relationship

The enhanced CO_2 resistance of $SrFeO_3$ by Sb doping is believed to originate from the structural changes of perovskite. The ionic potential, i.e., electric charge (*Z*) divided by the ionic radius (*r* in Å), is a measure of bond strength in the network.[43] Sb^{5+} (8.33) (ionic radius (*N*=6) is 0.6 Å[44]) has a much larger ionic potential than that of Fe^{3+} (4.65, hs) and Fe^{4+} (6.84), which would lead to stronger Sb-O bonds. This is in agreement with the calculated levels of oxygen vacancy formation energy for Fe-O-Sb and increased ABE by Sb doping. Since the reaction of CO_2 with the oxide requires an extra oxygen atom from the oxide for carbonate formation, the stabilization of the lattice oxygen by Sb^{5+} would be expected to improve the CO_2 resistance of the material. Moreover, the increased O1s binding energy observed by XPS, i.e., reduced electron cloud density for oxygen, may also be ascribed to the stronger attraction of Sb^{5+} than Fe^{3+}/Fe^{4+}. It is noteworthy that Sb doping also leads to some changes in the local structure around Fe cations. The decreased Fe oxidation state and larger Fe-O inter-atomic distance are generally unfavorable for the metal-oxygen bonding. Since these changes are minor, they may only partly counteract the positive effect of enhanced Sb-O bonding on the materials stability.

Likewise, the reduced oxygen reduction activity observed with Sb doping can be attributed to changes in the structural parameters. Oxygen transport in ionic solids is usually favoured by high concentration and high mobility of oxygen vacancies[45], which prefer a low energy barrier pathway. Sb-doped $SrFeO_3$ is associated with reduced oxygen vacancy concentration, with the oxygen vacancies preferring to be associated with Fe atoms due to the stronger bonding of Sb-O as compared to Fe-O. The lower oxygen mobility would result from the pinning of oxygen by Sb, which increases the energy barrier for oxygen transport and results in a longer and more tortuous transport pathway.

The above analyses show that the trade-off between the CO_2 resistance and ORR activity in $SrFe_{1-x}Sb_xO_3$ is, in fact, a result of their contradictory requirements for structural parameters. Strong B-O bonding favors high CO_2 stability, but inevitably reduces the concentration and mobility of oxygen vacancies resulting in decreased ORR activity, and vice versa. Therefore, to meet the demands of versatile applications, one needs to balance the stability and performance of perovskite-structured oxides. Since the perovskite structure allows for flexible compositions, this can in principle be achieved by fine tuning the materials' composition through appropriate choice of dopants.

4. Conclusions

In summary, a systematic experimental investigation of the stability-performance trade-off of antimony-doped $SrFeO_3$ cathode was performed. The resistance of the $SrFe_{1-x}Sb_xO_{3-\delta}$ oxides toward acidic CO_2 can be effectively increased by antimony doping which reduces secondary phase formation at the surface. On the other hand, stability-performance trade-off depends enormously on the structural changes of the perovskite oxides. Iron substitution by Sb results in a decrease of the oxygen vacancy concentration and iron oxidation state and a concomitant increase of the Fe-O atomic distance. Sb doping increases the bond strength due to its larger ionic potential and increases the energy barrier for oxygen migration. The enhanced stability of oxygen around Sb gives rise to enhanced CO_2 tolerance, while the suppressed oxygen mobility results in decreased levels of oxygen transport. The effect of CO_2 concentration on the oxygen surface exchange rate is also investigated. This work provides evidence and a path forward for the field to tailor the performance of perovskite-type cathodes of SOFCs through compositional modifications.

■ ACKNOWLEDGEMENTS

Financial support by the Natural Science Foundation of China (Grant Nos. 61871359, U1432108, 51572255, U1632131) is gratefully acknowledged. The authors thank beamline BL14W1 (Shanghai Synchrotron Radiation Facility) for providing the beam time. The authors also thank Dr. Wei Liu for assistance in the EXAFS data analyses. KSB was supported in part by an appointment to the National Energy Technology Laboratory Research Participation Program, sponsored by the U.S. Department of Energy and administered by the Oak Ridge Institute for Science and Education. KSB, JG, and YM also gratefully acknowledge the financial support from the Department of Energy, Nuclear Energy Research Program (DOE-NEUP) Project: 17-12798: Nanostructured Ceramic Membranes for Enhanced Tritium Management.

Supporting Information Available: In situ XRD patterns, Thermal expansion coefficient, Deconvolution of pre-edge XANES spectra, k^3-weighted EXAFS signals, Fourier-transformed and fitted EXAFS spectra, TGA for SFS20 in CO_2, Conductivity relaxation of SFS05, SEM, Oxygen permeation fluxes, Activation energies data are provided.

■ REFERENCES:

(1) Chen, Y.; Yoo, S.; Choi, Y.; Kim, J. H.; Ding, Y.; Pei, K.; Murphy, R.; Zhang, Y.; Zhao, B.; Zhang, W.; Chen, H.; Chen, Y.; Yuan, W.; Yang, C.; Liu, M. A Highly Active, CO_2 -Tolerant Electrode for the Oxygen Reduction Reaction. *Energy Environ. Sci.* **2018**, *11*, 2458–2466.

(2) Ding X.; Gao Z.; Ding D.; Zhao X.; Hou H.; Zhang S.; Yan G. Cation Deficiency Enabled Fast Oxygen Reduction Reaction for a Novel SOFC Cathode with Promoted CO_2 Tolerance. *Appl. Catal. B Environ.* **2019**, *243*, 546-555.

(3) Li J.; Zhang Q.; Qiu P.; Jia L.; Chi B.; Pu J.; Li J. A CO_2-Tolerant $La_2NiO_{4+\delta}$-Coated $PrBa_{0.5}Sr_{0.5}Co_{1.5}Fe_{0.5}O_{5+\delta}$ Cathode for Intermediate Temperature Solid Oxide Fuel Cells. *J. Power Sources* **2017**, *342*, 623-628.

(4) Yan, A.; Cheng, M.; Dong, Y.; Yang, W.; Maragou, V.; Song, S.; Tsiakaras, P. Investigation of a $Ba_{0.5}Sr_{0.5}Co_{0.8}Fe_{0.2}O_{3-\delta}$ Based Cathode IT-SOFC. *Appl. Catal. B Environ.* **2006**, *66*, 64–71.

(5) Yan, A.; Liu, B.; Dong, Y.; Tian, Z.; Wang, D.; Cheng, M. A Temperature Programmed Desorption Investigation on the Interaction of $Ba_{0.5}Sr_{0.5}Co_{0.8}Fe_{0.2}O_{3-\delta}$ Perovskite Oxides with CO_2 in the Absence and Presence of H_2O and O_2. *Appl. Catal. B Environ.* **2008**, *80*, 24–31.

(6) Zhou, W.; Liang, F.; Shao, Z.; Zhu, Z. Hierarchical CO_2-Protective Shell for Highly Efficient Oxygen Reduction Reaction. *Sci. Rep. 2* **2012**, *327*.

(7) Yan, A.; Yang, M.; Hou, Z.; Dong, Y.; Cheng, M. Investigation of $Ba_{1-x}Sr_xCo_{0.8}Fe_{0.2}O_{3-\delta}$ as Cathodes for Low-Temperature Solid Oxide Fuel Cells Both in the Absence and Presence of CO_2. *J. Power Sources* **2008**, *185*, 76–84.

(8) Zeng, Q.; Zuo, Y.; Fan, C.; Chen, C. CO_2-Tolerant Oxygen Separation Membranes Targeting CO_2 Capture Application. *J. Membr. Sci.* **2009**, *335*, 140–144.

(9) Zhu, J.; Guo, S.; Chu, Z.; Jin, W. CO_2-Tolerant Oxygen-Permeable Perovskite-Type Membranes with High Permeability. *J. Mater. Chem. A* **2015**, *3*, 22564–22573.

(10) Yi, J.; Schroeder, M.; Martin, M. CO_2-Tolerant and Cobalt-Free $SrFe_{0.8}Nb_{0.2}O_{3-\delta}$ Perovskite Membrane for Oxygen Separation. *Chem. Mater.* **2013**, *25*, 814–817.

(11) Yi, J.; Brendt, J.; Schroeder, M.; Martin, M. Oxygen Permeation and Oxidation States of Transition Metals in (Fe, Nb)-Doped $BaCoO_{3-\delta}$ Perovskites. *J. Membr. Sci.* **2012**, *387–388*, 17–23.

(12) Zhang, Y.; Gao, X.; Sunarso, J.; Liu, B.; Zhou, W.; Ni, M.; Shao, Z. Significantly Improving the Durability of Single-Chamber Solid Oxide Fuel Cells: A Highly Active CO_2-Resistant Perovskite Cathode. *ACS Appl. Energy Mater.* **2018**. *1*, 1337-1343.

(13) Park, J. H.; Kim, K. Y.; Park, S. D. Oxygen Permeation and Stability of $La_{0.6}Sr_{0.4}Ti_xFe_{1-x}O_{3-\delta}$ (x=0.2 and 0.3) Membrane. *Desalination* **2009**, *245*, 559–569.

(14) Klande, T.; Ravkina, O.; Feldhoff, A. Effect of A-Site Lanthanum Doping on the CO_2 Tolerance of $SrCo_{0.8}Fe_{0.2}O_{3-\delta}$ Oxygen-Transporting Membranes. *J. Membr. Sci.* **2013**, *437*, 122–130.

(15) Efimov, K.; Klande, T.; Juditzki, N.; Feldhoff, A. Ca-Containing CO_2-Tolerant Perovskite Materials for Oxygen Separation. *J. Membr. Sci.* **2012**, *389*, 205–215.

(16) Yi, J.; Schroeder, M.; Weirich, T.; Mayer, J. Behavior of Ba(Co, Fe, Nb)$O_{3-\delta}$ Perovskite in CO_2-Containing Atmospheres: Degradation Mechanism and Materials Design. *Chem. Mater.* **2010**, *22*, 6246–6253.

(17) Schulze-Küppers, F.; ten Donkelaar, S. F. P.; Baumann, S.; Prigorodov, P.; Sohn, Y. J.; Bouwmeester, H. J. M.; Meulenberg, W. A.; Guillon, O. Structural and Functional Properties of $SrTi_{1-x}Fe_xO_{3-\delta}$ ($0\leqslant x\leqslant 1$) for the Use as Oxygen Transport Membrane. *Sep. Purif. Technol.* **2015**, *147*, 414–421.

(18) Chen, W.; Chen, C.; Winnubst, L. Ta-Doped $SrCo_{0.8}Fe_{0.2}O_{3-\delta}$ Membranes: Phase Stability and Oxygen Permeation in CO_2 Atmosphere. *Solid State Ion.* **2011**, *196*, 30–33.

(19) Han, Y.; Yi, J.; Guo, X. Improving the Chemical Stability of Oxygen Permeable $SrFeO_{3-\delta}$ Perovskite in CO_2 by Niobium Doping. *Solid State Ion.* **2014**, *267*, 44–48.

(20) Beyer H.; Metzger M.; Sicklinger J.; Wu X.; Schwenke U. K.; Gasteiger A. H. Antimony doped Tin oxide-synthesis, characterization and application as cathode material in Li-O_2 cells: implications on the prospect of carbon-free cathodes for rechargeable Lithium-air batteries. *J. Electrochem. Soc.* **2017**, *164*, A1026-A1036.

(21) Yan L.; Liu Y.; Hu H.; Li H.; Shi L.; Zhang D. Investigations on the Antimony Promotional Effect on CeO_2-WO_3/TiO_2 for Selective Catalytic Reduction of NO_x with NH_3. *ChemCatChem.* **2016**, *8*, 2267-2278.

(22) Zhu, Y.; Sunarso, J.; Zhou, W.; Shao, Z. Probing CO_2 Reaction Mechanisms and Effects on the $SrNb_{0.1}Co_{0.9-x}Fe_xO_{3-\delta}$ Cathodes for Solid Oxide Fuel Cells. *Appl. Catal. B Environ.* **2015**, *172–173*, 52–57.

(23) Shao, Z. Investigation of the Permeation Behavior and Stability of a $Ba_{0.5}Sr_{0.5}Co_{0.8}Fe_{0.2}O_{3-\delta}$ Oxygen Membrane. *J. Membr. Sci.* **2000**, *172*, 177–188.

(24) J.A. Kilner; R.J. Brook. A Study of Oxygen Ion Conductivity in Doped Non-Stoichiometric Oxides. *Solid State Ion.* **1982**, *6*, 237–252.

(25) Zhang, Y.; Yang, G.; Chen, G.; Ran, R.; Zhou, W.; Shao, Z. Evaluation of the CO_2 Poisoning Effect on a Highly Active Cathode $SrSc_{0.175}Nb_{0.025}Co_{0.8}O_{3-\delta}$ in the Oxygen Reduction Reaction. *ACS Appl. Mater. Interfaces* **2016**, *8*, 3003–3011.

(26) Huang, Y.-L.; Pellegrinelli, C.; Sakbodin, M.; Wachsman, E. D. Molecular Reactions of O_2 and CO_2 on Ionically Conducting Catalyst. *ACS Catal.* **2018**, *8*, 1231–1237.

(27) Ravel, B.; Newville, M. *ATHENA, ARTEMIS*, *HEPHAESTUS*: Data Analysis for X-Ray Absorption Spectroscopy Using *IFEFFIT*. *J. Synchrotron Radiat.* **2005**, *12*, 537–541.

(28) Newville, M. *IFEFFIT*: Interactive XAFS Analysis and *FEFF* Fitting. *J. Synchrotron Radiat.* **2001**, *8*, 322–324.

(29) Kresse, G.; Hafner, J. *Ab Initio* Molecular Dynamics for Open-Shell Transition Metals. *Phys. Rev. B* **1993**, *48*, 13115–13118.

(30) Kresse, G.; Furthmüller, J. Efficient Iterative Schemes for *Ab Initio* Total-Energy Calculations Using a Plane-Wave Basis Set. *Phys. Rev. B* **1996**, *54*, 11169–11186.

(31) Kobayashi, G.; Nishimura, S.; Park, M.-S.; Kanno, R.; Yashima, M.; Ida, T.; Yamada, A. Isolation of Solid Solution Phases in Size-Controlled Li_xFePO_4 at Room Temperature. *Adv. Funct. Mater.* **2009**, *19*, 395–403.

(32) Ullmann, H.; Trofimenko, N.; Tietz, F.; Stöver, D.; Ahmad-Khanlou, A. Correlation between Thermal Expansion and Oxide Ion Transport in Mixed Conducting Perovskite-Type Oxides for SOFC Cathodes. *Solid State Ion.* **2000**, *138*, 79–90.

(33) John R. Anderson; Michel Boudart. Catalysis: Science and Technology. *Springer Sci. Bus. Media*, Berlin, **2012**, 1-312.

(34) Gyu Kim, M.; Sang Cho, H.; Hyun Yo, C. Fe K-Edge X-Ray Absorption (XANES/EXAFS) Spectroscopic Study of the Nonstoichiometric $SrFe_{1-x}Sn_xO_{3-y}$ System. *J. Phys. Chem. Solids* **1998**, *59*, 1369–1381.

(35) Westre, T. E.; Kennepohl, P.; DeWitt, J. G.; Hedman, B.; Hodgson, K. O.; Solomon, E. I. A Multiplet Analysis of Fe K-Edge 1s → 3d Pre-Edge Features of Iron Complexes. *J. Am. Chem. Soc.* **1997**, *119*, 6297–6314.

(36) Petit, P.-E.; Farges, F.; Wilke, M.; Solé, V. A. Determination of the Iron Oxidation State in Earth Materials Using XANES Pre-Edge Information. *J. Synchrotron Radiat.* **2001**, *8*, 952–954.

(37) Waychunas, G. A.; Apted, M. J.; Brown, G. E. X-Ray K-Edge Absorption Spectra of Fe Minerals and Model Compounds: Near-Edge Structure. *Phys. Chem. Miner.* **1983**, *10*, 1–9.

(38) Tassel, C.; Kageyama, H. Square Planar Coordinate Iron Oxides. *Chem Soc Rev* **2012**, *41*, 2025–2035

(39) Radaelli, P. G.; Iannone, G.; Marezio, M.; Hwang, H. Y.; Cheong, S.-W.; Jorgensen, J. D.; Argyriou, D. N. Structural Effects on the Magnetic and Transport Properties of Perovskite $A_{1-x}A_{x}'MnO_3$ (x=0.25, 0.30). *Phys. Rev. B* **1997**, *56*, 8265–8276.

(40) Zhang, G.; Liu Z.; Zhu N.; Jiang W.; Dong X.; Jin W. A Novel Nb_2O_5-doped $SrCo_{0.8}Fe_{0.2}O_{3-\delta}$ Oxide with High Permeability and Stability for Oxygen Separation. *J. Membr. Sci.* **2012**, *405-406*, 300-309.

(41) Yu X.; Long W.; Jin F.; He T. Cobalt-free Perovskite Cathode Materials $SrFe_{1-x}Ti_xO_{3-\delta}$ and Performance Optimization for Intermediate-Temperature Solid Oxide Fuel Cells. *Electrochemica Acta* **2014**, *123*, 426-434.

(42) Xia, C. Low-Temperature SOFCs Based on $Gd_{0.1}Ce_{0.9}O_{1.95}$ Fabricated by Dry Pressing. *Solid State Ion.* **2001**, *144*, 249–255.

(43) Shartsis, L.; Spinner, S.; Capps, W. Density, Expansivity, and Viscosity of Molten Alkali Silicates. *J. Am. Ceram. Soc.* **1952**, *35*, 155–160.

(44) R. D. Shannon. Revised Effective Ionic Radii and Systematic Studies of Interatomic Distances in Halides and Chalcogenides. *Acta Crystallogr. Sect. A* **1976**, *32*, 751–767.

(45) M. Cherry; M. S. Islam; C. R. A. Catlow. Oxygen Ion Migration in Perovskite-Type Oxides. *J. Solid State Chem.* **1995**, *118*, 125–132.

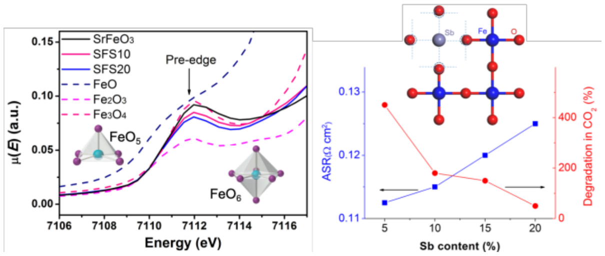
SrFeO3
SFS10
SFS20
FeO
Fe2O3
Fe3O4
Pre-edge
FeO5
FeO6
μ(E) (a.u.)
0.15
0.10
0.05
0.00
7106
7108
7110
7112
7114
7116
Energy (eV)
Sb
Fe
O
ASR(Ω cm²)
0.13
0.12
0.11
Degradation in CO2 (%)
400
200
0
5
10
15
20
Sb content (%)

TOC